Improved heat transfer for pyroelectric energy harvesting applications using a thermal conductive network of aluminum nitride in PMN-PMS-PZT ceramics

Qingping Wang[a,b], Chris R. Bowen[c], Wen Lei[a], Haibo Zhang[a], Bing Xie[a], Shiyong Qiu[a], Mingyu Li[a,], Shenglin Jiang[a,]

[a]*School of Optical and Electronic Information, Huazhong University of Science and Technology, Wuhan 430074, PR China*

[b]*Department of Physics & Mechanical and Electronic Engineering, Hubei University of Education, Wuhan 430205, PR China*

[c]*Materials Research Centre, Department of Mechanical Engineering, University of Bath, Claverton Down Road, Bath BA2 7AY, UK*

Abstract: The harvesting of waste heat is attracting increasing attention, due to its abundance and potential benefits to the environment. However, the need for high heat transfer rates in thermal harvesting systems is a longstanding obstacle for their practical application. In this work, we construct thermally conductive networks in $Pb[(Mn_xNb_{1-x})_{1/2}(Mn_xSb_{1-x})_{1/2}]_y(Zr_{95}Ti_5)_{1-y}O_3$ (lead magnesium niobate-lead antimony-manganese-lead zirconate titanate: PMN-PMS-PZT) ceramics to improve heat transfer and enhance their ferroelectric properties by use of a thermally conductive AlN additive dispersed in the ceramic matrix. The ferroelectric properties, pyroelectric coefficient and thermal conductivity of the PMN-PMS-PZT: AlN composite materials are influenced by the AlN content as a result of the formation of random bridges or thermally conductive networks for phonon transfer in the ceramic matrix, thereby leading to high heat transfer. For a PMN-PMS-PZT composite with a 0.2 wt. % AlN content, the ferroelectric properties, pyroelectric coefficient and thermal conductivity are shown to be enhanced owing to the improved crystallinity and density, and the relative permittivity is also reduced, which results optimized pyroelectric figure of merits. This combination of materials property enhancements is shown to be beneficial for high performance pyroelectric materials in devices for energy harvesting applications.

Key words: AlN, pyroelectric ceramic, electrical properties, energy harvesting

1. Introduction

Energy harvesting, or energy scavenging, is a technique for converting ambient forms of energy such as light, heat, wind, vibration, and human movement into useful electrical energy. The harvesting field continues to receive significant interest[1-3], since it offers a fundamental energy solution for small-power applications including, but not limited to, ubiquitous wireless sensor nodes, portable and wearable electronics, and structural/environmental monitoring devices. Among the variety of potential sources of ambient energy available, the harvesting of thermal energy is considered to be a highly promising technology due to the significant amounts of waste heat and temperature flucuations in industrial processes and in the environment[2].

Thermal-electric energy harvesting relies on two main principles: the Seebeck effect and the pyroelectric effect. The Seebeck effect utilizes a spatial temperature difference (dT/dx) to drive the diffusion of charge carriers in order to convert heat into electricity[3]. Usually, natural temperature-time variations result in a thermal energy with an unstable spatial temperature gradient, which is difficult to transform into electrical energy using thermoelectric modules. In contrast to thermoelectric generators, pyroelectric materials do not need a spatial temperature gradient, and have the ability to convert temperature fluctuations (dT/dt) into electrical power with a potentially higher thermodynamic efficiency[2]. Energy conversion by heating and cooling a pyroelectric material therefore offers a novel way to convert heat into electricity and the approach has promising applications for self-powered devices and battery-free wireless sensors[4]. A number of researchers have made efforts to improve the efficiency of energy conversion, by enhancing the pyroelectric properties of materials[1, 5, 6], the design of structures with high heat transfer rates [7-11], and optimizing the energy collection and storage circuits[2, 12-15].

Unfortunately, the reported power levels during thermal energy conversion using pyroelectric materials remain low, which limits potential applications for energy harvesting. The current produced by the pyroelectric cell is based on the pyroelectric

effect, which converts temperature variations into a corresponding electric output. The generated pyroelectric current (I_p), at short circuit conditions, is given by[9]:

$$I_p = dQ_p/dt = A \cdot p \cdot dT/dt \quad (1)$$

Where Q_p is the pyroelectric charge, A is the electrode area, dT/dt is the rate of temperature change and p is the pyroelectric coefficient given by:

$$p = dP_s/dT \quad (2)$$

Where P_s is the spontaneous polarization[2]. Clearly, to maximize the pyroelectric current under short-circuit conditions, the pyroelectric cell should have a large electrode area, a high pyroelectric coefficient and a high rate of temperature change.

Recently, materials with improved heat transfer, which can increase the dT/dt have been reported and this has also included effort to improve the p and relevant pyroelectric figures of merit (FOMs) for energy harvesting applications. For instance, Hsiao et al. explored the potential to improve the pyroelectric conversion efficiency of lead zirconate titanate (PZT) plates by increasing its temperature variation rate[16]. A 55% higher temperature variation rate was achieved by trenching a PZT material in a thicker PZT cell[17] and a 53.9% larger temperature variation was obtained by using a sandblasting etching technique to fabricate a vortex-like electrode compared to the fully covered type[18]. More recently, Bowen et al. made contributions to enhance the heat transfer of a pyroelectric energy harvester using a meshed electrode and micropattering the surface of pyroelectric materials[19], as well as developing porous PZT ceramics with tailored and aligned porosity[1]. Although these techniques were demonstrated to achieve a substantial improvement in the output power through the enhancement of heat transfer and pyroelectric properties, it is observed that the output voltage, current for pyroelectric cell, and overall power levels, are still relatively low. There has been limited work on attempting to enhance the temperature response by constructing a thermally conductive network to improve the heat transfer throughout the pyroelectric material. In this paper, the p and the dT/dt of a PMN-PMS-PZT ceramic were increased by using AlN as a high thermal conductivity filler which also aids densification and improves the ferroelectric properties. This combination of

property changes leads to increased output power for energy harvesting applications compared to the pure ferroelectric material.

In principle, the rate of heat transfer involves the transport of energy from one place to another by energy carriers. In solid materials, phonons, electrons, or photons are responsible for transporting energy. Phonons, which are quantized modes of vibration occurring in a rigid crystal lattice, are the primary mechanism of heat conduction in the majority of electrically insulating materials since the free movement of electrons is not possible[20]. As the thermal conductivity plays a key role for heat transfer, there is a need to increase it for pyroelectric materials to improve *dT/dt*. In order to improve the thermal conductivity, filler particles with high thermal conductivity are often dispersed into the material to form a thermally conductive network that improves the transportation of phonons, which can be considered as a heat transfer network[20-26].

Many high thermal conductivity ceramic fillers such as diamond, beryllia (BeO), aluminum nitride (AlN), and aluminum oxide (Al_2O_3) have been incorporated into a thermally insulating matrix to form composites with improved thermal properties. Diamond is the ideal solid filler for heat conduction, however it is expensive, and BeO is toxic. The theoretical thermal conductivity of Al_2O_3 (30 W/mK) is lower than that of AlN (320 W/mK). In addition, aluminum nitride (AlN) possesses high thermal conductivity, is electrically insulating, non-toxic, has a stable crystal structure, and is relatively low cost[24, 27]. For example, the thermal conductivity of composite phase change materials (PCMs) was examined and the thermal conductivity of β-aluminum nitride as a heat transfer promoter was investigated. The results showed that the thermal conductivity of the composite PCMs increased with increasing β-aluminum nitride content[23]. Recently, a thermally conductive filler/epoxy resin (EP) composite was investigated which indicated that the thermal conductivity of all composites were enhanced with an increase in the amount of thermal conductive AlN filler[25]. AlN particles were used as thermally conductive filler to fabricate conductive adhesives and the results showed that the thermal conductivity of adhesive was approximately 11.8 times higher than that of pure epoxy, when 70 wt. % of 5um size AlN particles

were added. However, to date, the effect of AlN filler on the thermal conductivity of ferroelectric ceramics and their electrical properties, such as pyroelectric coefficient, and relative permittivity for energy harvesting applications has yet to be reported.

In this work, we utilize a two-step sintering method to fabricate $Pb[(Mn_xNb_{1-x})_{1/2}(Mn_xSb_{1-x})_{1/2}]_y(Zr_zTi_{1-z})_{1-y}O_3$ (PMN-PMS-PZT): xAlN ceramics to produce high thermal conductivity composite materials for pyroelectric energy harvesting applications. A systematic investigation is conducted on the effect of the AlN content in the PMN-PMS-PZT ceramics for heat transfer and its impact on dielectric and ferroelectric properties. The pyroelectric coefficient and thermal conductivity of the ceramics are measured and the results show that the sample with 0.2 wt. % AlN additions generates more energy compared with the pristine PMN-PMS-PZT material. Our work demonstrates that the pyroelectric ceramic with AlN additions can improve the heat transfer and energy generation for harvesting devices.

2. Experimental

$Pb[(Mn_xNb_{1-x})_{1/2}(Mn_xSb_{1-x})_{1/2}]_y(Zr_zTi_{1-z})_{1-y}O_3$ pyroelectric ceramics were prepared initially by a solid-state reaction technique[5], Stoichiometric PbO (99.0%), ZrO_2(99.9%), TiO_2 (99.8%), Nb_2O_5(99.5%), and Sb_2O_3(99.0%, all from Sinopharm Chemical Reagent Co., Ltd, China) were utilized as the starting raw materials. $Mn(NO_3)$ (50%, from Sinopharm Chemical Reagent Co., Ltd, China) and deionized water were used as solvents. A 10 mol% excess of PbO was introduced to compensate for lead loss during the high-temperature sintering and to prevent the formation of pyrochlore phase[5] in the ceramics. These precursors were initially ball milled for 4h, and then heated in a furnace at 100 ˚C/ for 1 h. The dry slurries were then heated in air at 700 ˚C for 3 h with a ram rate of 5˚C/min to burn out the organic additives. After the drying process, the powders were ground by hand and ball milled again in deionized water for 4h. The PMN-PMS-PZT powders were obtained using a sintering at 1230 ˚C for 4h under a Pb-rich atmosphere followed by the natural cooling. A high degree of crystallinity was observed for the powders, as shown in Fig. S1 (a), and the

powders were crystallized as the pure perovskite phase, as shown in Fig. S1 (b). The prepared PMN-PMS-PZT powders were mixed with various contents of commercial AlN particles (99.5%, from Aladdin) with a particle size of 1.55 μm with a fraction x=0, 0.1, 0.2, 0.3 and 0.5 wt. %. The surface morphology and crystal structure of the AlN particles are shown in Fig.S2. Each series was ball milled again in deionized water for 4h, and subsequently pressed into a disk with a diameter of 10 mm under 8 MPa using 8 wt. % polyvinyl acetate (PVA) as a binder after drying. Sintering was carried out in covered alumina crucibles at 1070 °C for 2h in air with a rapid increasing and decreasing temperature rate of 8 °C/min.

X-ray diffraction patterns for all samples were performed by using a PANalytical X'Pert-PRO diffractometer with $CuK_{\alpha 1}$ radiation. The microstructures and the energy-dispersive spectra were characterized by field-emission scanning electron microscopy (FE-SEM Sirion200) and energy-dispersive X-ray spectroscopy (EDS). The element distribution was examined by electron probe microanalyzer (EPMA-8050G, SHIMADZU, Japan).

For characterization of electrical properties, the fabricated samples with a diameter of ~ 8.5 mm were painted with silver electrodes with a thickness of ~ 0.3 mm on both sides, and treated with a 600°C heating process for 25 min. All samples were poled under a 30 kV/cm DC field at 120 °C for 30 min in silicone oil and aged for 24 h before testing. The relative permittivity (ε_r) and loss tangent ($\tan\delta$) were measured using an impedance analyzer (HP4294A) on unpoled samples at a range of frequencies between 1 kHz to 10 MHz at 300 °C and in a temperature range from 30 °C to 300 °C at each frequency. Polarization versus electric field (P-E) hysteresis loops were obtained at 10 Hz using a PMF1011-277 system. The pyroelectric short circuit current were measured by an electrometer (Picoammeter 6485, Keithley Instruments, Cleveland, OH), and the pyroelectric coefficient was obtained using a standard Byer-Roundy method via an in-house pyroelectric parameter tracer. The thermal diffusivity (α) and specific heat capacity (C_p) of the samples were measured with the graphite-coated cylindrical specimen with an average thickness of 1 mm and 127 mm in diameter in the interval from 20 to 60 °C by laser flash analysis using a

LFA427 Microflash (NETZSCH-Gerätebau GmbH, Germany). The density of the samples (ρ) were characterized by the Archimedes method.

To study the materials for pyroelectric energy harvesting, two Peltier cells were employed as the heat source for heating and cooling the samples. Two K-type thermocouples were applied to monitor the temperature of the hot/cold flow and a heat sink and fan were utilized to cool the device. A PC-based data acquisition system was employed to record the output current and voltage of the pyroelectric energy harvesters. The required data finally was acquired with LabVIEW and a data acquisition card.

3. Results and Discussion

3.1 Microstructure characterization

Figure 1(a) shows the XRD patterns of the samples at room temperature, which were recorded with a step size of 0.02° at a scanning rate of 8°/min within 2θ from 10° to 80°. The presence of sharp and well-defined peaks indicate that all the samples were in the perovskite phase with a good degree of crystallinity, while the presence of weak peaks at 28.15° was due to the PbO secondary phase, as seen in Fig. 1(b). With an increase in AlN content, the PbO phase disappeared, which suggested that AlN can be effective for inhibiting the formation of pyrochlore phase[5, 27]. In addition, a similar phase distribution was observed in samples with x=0.15, 0.25 and 1.0, as shown in Fig. S3.

Figure 2 shows the morphological evolution of the PMN-PMS-PZT:xAlN samples with various AlN contents from 0 to 0.5 wt.%. Initially, the sample with x = 0 appeared with relatively densely packed grains and less defects, see Figure 2a. When the AlN content increased to 0.1 wt%, pores and defects were observed in the sample that originated from the differences in size and interatomic forces between impurity and host atoms[27], as shown in Figure 2b. When the AlN content reached 0.2 wt. %, the surface morphology became more dense with a increased grain size, which can be a result of enhanced crystallization when the Al and N ions entered into the lattice[26]. With a further increase in AlN content beyond 0.2wt.%, defects and pores gradually

appear, which can be ascribe to the partial melting of the crystal grains due to the increased temperature along with the additional AlN contents in lattice[22]. As a result, the mean diameter of the grains gradually evolved as a function of the AlN contents as shown in Fig. 2(f), and a similar trend can be also observed the samples with x=0.15, 0.25 and 1.0 wt. % as shown in Fig.S4.

Figure 3 and Figure S5 show the elemental analysis of the PMN-PMS-PZT sample with 0.2 wt. % AlN with 2 and 5 μm scale bars, respectively. The elemental distribution of the pristine PMN-PMS-PZT sample are shown in Fig. S6. As clearly shown in Fig. 3(b), 3(d), and 3(f), the elements Pb, Zr, and O were evenly distributed in the material. Similarly, N was also observed in the sample, as shown in Fig. 3(e), nevertheless Al only appeared at the grain boundaries as seen by examination of Figs. 3(a) and 3(c). The higher concentration of Al at the grain boundaries may be due to limited diffusion of Al atoms in the ceramic matrix. While, N atoms can be more easily thermally activated for diffusion, thus resulting in a more uniform distribution. For the pristine sample, each element was uniformly distributed in the sample, as clearly shown in Fig. S6. The energy dispersive spectrum of the PMN-PMS-PZT sample with 0.2 wt. % AlN is shown in Fig. 3(g). The peaks of N and Al are noticeably observed at 0.39 and 1.49 keV, respectively, which can be an evidence for the existence of AlN, where the AlN is located at grain boundaries and some N has diffused into ceramic matrix.

3.2 Dielectric properties

Figures 4(a) and 4(b) show the relative permittivity (ε_r) and loss tangent (tanδ) of the unpoled materials measured within a systematic temperature variation between 30 and 300 °C at a fixed frequency of 1 kHz. The frequency dependent ε_r and tanδ of the corresponding samples within the temperature range of 30 - 300 °C are shown in Figs. 4(c) and 4(d), respectively. The temperature dependent behavior of the ε_r and tanδ of the samples with 0.15, 0.25, and 1.0 wt. % AlN contents are shown in Fig. S7. As can be seen in Fig. 4(a), all samples exhibited a single dielectric peak during the heating process, which was typical of a phase transition. For each sample, as shown in Fig.

4(a), the ε_r first gradually increased with elevated temperature, indicating the ferroelectric phase existence before the Curie temperature point at 209.2, 211.2, 211.7, 209.5, and 211.2°C for samples with x=0, 0.1, 0.2, 0.3 and 0.5 wt.% AlN content, respectively. The ε_r subsequently decreased above the Curie temperature, which can be induced by the transition from a ferroelectric phase to a paraelectric phase[28]. The Curie temperature remained almost constant except for the sample with AlN content of 0.2 wt. %, which exhibited the lowest relative permittivity (ε_r) as shown in Fig. 4(a), suggesting a more difficult polarization due to a comparably higher density. A similar behavior can be witnessed with the tanδ as a function of AlN when the temperature was increased as shown in Fig.4 (b). The tanδ for each sample was comparable and less than 0.02 at temperatures below 100°C. As shown in Fig. 4(c), the ε_r gradually decreased with increased frequency at each temperature, which was induced by the different response times for the various dipoles[6]. In addition, a more stable tanδ can be obtained at relatively high frequencies due to a greater contribution of electrical conductivity to the loss at low frequencies, as shown in Fig. 4(d).

3.3 Ferroelectric properties and pyroelectric properties

Figure 5(a) shows the P-E loops measured within an identical variation of the electric field, and the corresponding values of P_S and P_r with increasing AlN content are shown in Fig. 5(b). The room temperature ferroelectric properties of the samples with 0.15, 0.25 and 1.0 wt.% AlN contents are shown in Fig.S8. In geneal, the coercive field (E_c) for each sample was relatively low, and the *Ps* and *Pr* were more sensitively to the AlN content, as shown in Fig. 5(a) and (b). Specificily, the P_s initially decreased from 23.9 to 20.72 μC/cm^2 as the AlN content increased to 0.1 wt.%, as shown in Fig. 5(b) and Table 1, which can be due to the decreased density of the resulting sample, see Fig. 2(f)[26]. As the AlN content increased to 0.2 wt.%, the P_s sharply increased to 26.59 μC/cm^2 at an applied electric field of 120 kV/cm owing to the improved domains switching along the polarization direction due to the enhanced crystalinity[29]. With a further increase in AlN content, the P_s then begins to decrease again from 22.7 to 19.21 μC/cm^2 , see Fig. 5(b), due to the increased defects between

domain walls[30]. In terms of P_r, it was observed to increase from 13.06 to 14.47 μC/cm^2 as the AlN content was increased to 0.1 wt.%,, as shown in Fig. 5(b) and Table 1, which can be induced by the effect of the pinning force for the domains switching due to the formation of the defects[30]. As mentioned, the crytallization has been enhanced with the formation of the thermally conductivity networks when the AlN content was 0.2 wt.%, which can weaken the pinning force for the domains switching and the remnant polarization of the sample increase at 0.2 wt.%. AlN. For AlN contents above 0.2wt.% the remnant polarization of the sample decreased, the P_r decreased significantly from 15.06 to 9.13 μC/cm^2, when the AlN contents increased from 0.3 to 0.5 wt.%. Similar trends of the P_r and P_s can be also observed with the AlN contents of 0.15, 0.25, and 1.0 wt.%, as shown in Fig. S6 and Table 1. In addition, the coercive field (E_c) of the pristine PMN-PMS-PZT exhibited a relatively small value (15.51kV/cm) while the E_c of the other samples remained larger, as shown in the inset of Fig.5(a). This is possibly due to the domain walls being pinned by the additional defects and AlN additions, thereby increasing the hardness for the P_r domains to reverse and increasing E_c[31].

Figures 6(a) and 6(b) show the pyroelectric coefficients (p) and the corresponding values measured in a temperature range of 28 to 52°C. As seen in Fig. 6(b), the values of p exhibited a similar trend with P_s. Initially, when the AlN content was 0.1 wt. %, the p decreased from 3767 to 3249 μC/m^{2}K as result of the reduced P_s. Afterwards, with 0.2 wt.% AlN content, the heat conductive network had formed and the pyroelectric response was obviously enhanced with a value of 4146 μC/m^{2}K due to the enhanced P_s. Finally, with a further addtion of AlN, the p dercreased again from 3346 to 3037 μC/m^{2}K owing to the reduction of P_s. Further, the peak value of p firstly appeared at 32.7°C and had a small shift to a lower temperature compared to that of the pristine PMN-PMS-PZT at 32.8°C, which can be explained that the pyroelectric response became weak due to the defects in this sample and increased porosity (see Figure 2). When the AlN increased to 0.2 wt. %, the temperature of the peak p moved to 31.6°C and when the AlN content increased to 0.3 and 0.5 wt. %, the temperatures of the peak p appeared at 33.2 and 33.4°C, respectively, which was ascribed to the

slower response of temperature due to a relatively poor microstructure with defects and holes (see Figure 2). The p of the materials with x=0.15, 0.25 and 1.0 were also measured, as shown in Fig.S8b, and the property values are listed on Supplementary Table 1. When compared with the pristine PMN-PMS-PZT ceramic, the p of PMN-PMS-PZT: 0.2AlN has a 10% increment, while the ε_r also shows a 11.8% reduction. The enhanced pyroelectric coefficient together with the reduced dielectric constant leads to the highest pyroelectric FOMs (such as $F_E' = p^2/\varepsilon C_V^2$ and $F_E = p^2/\varepsilon$) for PMN-PMS-PZT: 0.2AlN ceramics compared with their counterparts[6].

3.4 Mechanism of heat transfer

In order to study the thermal conductivity of the samples for heat transfer and pyroelectric energy harvesting, the temperature dependence of thermal conductivity was investigated from 25°C to 60°C, as shown in Figure 7(a). The thermal conductivity can be calculated according to the following equation:

$$K=\alpha\rho C_p \quad (3)$$

Where α is the thermal diffusivity, ρ is the density and C_p is the specific heat capacity. As can be seen from Fig. 7(a), the thermal conductivity for each sample is relatively insensitive to temperature. However, it firstly decreased from 0 to 0.1 wt. % of AlN, then increased to a maximum when the AlN content was 0.2 wt.% and finally decreased rapidly for 0.3 and 0.5 wt.%. This behavior is similar to the variation in sintered density, as seen in Figure 7(b). Theoretically, the thermal resistance is a result of phonon scattering, thus it has to be minimized to increase thermal conductivity. Ceramics with high thermal conductivities can be obtained by using fillers with high intrinsic conductivities[21]. When the content of AlN is 0.1 wt.%, the formation of the thermally conductive channels is not possible while the density of the sample decreased due to the point defect scattering originated from the differences in size and interatomic forces between impurity and host atoms[27]. When the AlN content was increased to 0.2 wt.% and 0.25 wt.%, the thermal conductivity reached 0.714 W/m°C and 0.726 W/m°C (Supplementary Table 1) which improved the conductivity by 9.3%

and 11.1% respectively, compared with pristine PMN-PMS-PZT. The formation of random bridges or networks from heat conductive particles facilitates phonon transfer leading to high conductivities[24, 26] and this heat transfer model is shown in Fig. 7(c). When the content of AlN increased to 0.3 wt. % and 0.5 wt. %，the thermal conductivity gradually decreased since excessive additions of AlN yields poor microstructures, as in aforementioned part in Fig. 2(e) and Fig. S4(c), which broke the thermal path and the phonon was deflected and scattered during the process of transmission in the samples[21], thereby the thermal conductivity decreased rapidly. The mechanism of heat transfer in samples is shown in Fig.7 (d). In a pure PMN-PMS-PZT ceramic, the PMN-PMS-PZT matrix is considered as a thermally homogeneous material. Thus, heat as the thermal wave diffused through it uniformly and slowly. After the addition of AlN fillers, the compatibility between the matrix and the fillers caused the thermal energy transfer from the matrix to the high thermal conductivity fillers. Moreover, owing to the vibrations of whole chain and phonon scattering, the heat transfer through the crystalline filler is efficient[25]. Therefore, the AlN filler is the main factor for determining the enhancement of thermal conductivity.

3.5 Pyroelectric energy harvesting

To assess the materials for pyroelectric harvesting, Figure 8(a) illustrates the measurement setup with the temperature range from 20°C to 50°C as shown in Fig. S9 (a). Two thin layers of Cu were utilized as top and bottom electrodes which helps to effectively transfer induced electrons from polarization fluctuation of the PMN-PMS-PZT: xAlN ceramics to an external circuit. The pyroelectric element is represented by a current source in parallel with a capacitor and resistor as shown in Fig. 8b[2, 4, 14]. The load resistor was 10MΩ, which was connected for impedance matching and the output voltage, *U*, was measured with LabVIEW software connected to the voltage follower (LM324) and data acquisition card as shown in Fig. 9. It can be clearly seen that on increasing the content of AlN from 0 to 0.5 wt.%, the sample with 0.1 wt.% AlN produced a decreased voltage, then increased to the

maximum when the content of AlN was 0.2 wt.% and finally decreased rapidly in the samples with 0.3 and 0.5 wt.% AlN, respectively. Further, the rate of temperature change had the similar trend of change. The peak voltage for the sample 0.2 wt.% AlN was 8.72 V and the corresponding current was 0.872 uA. The power (*P*), calculated according to the equation $P=UI$ was 7.6 uW. The pristine PMN-PMS-PZT ceramic has a voltage of 7.05 V, current (0.705 uA) and power (4.97 uW). The peak rate of voltage change (dT/dt) for the sample 0.2 wt. % AlN was 3.32 °C/s which demonstrated the fastest pyroelectric response speed. The output voltages and the rates of temperature change of the samples with 0.15, 0.25 and 1.0 wt. % AlN were also demonstrated in Fig. S9 (b), (c) and (d), respectively. The detail parameters of all samples for energy harvesting are listed on supplementary Table 2 and we can see that the peak voltage (8.72 V) for the sample with 0.2 wt. % AlN was 24.6% higher than that of the pristine PMN-PMS-PZT (7V). This clearly verifies that the addition AlN helps to enhance the heat transfer for pyroelectric energy harvesting, and the improved pyroelectric figure of merit also improves the energy generated.

4. Conclusions

This paper presents the design and fabrication of novel high performance $Pb[(Mn_xNb_{1-x})_{1/2}(Mn_xSb_{1-x})_{1/2}]_y(Zr_zTi_{1-z})_{1-y}O_3$ (PMN-PMS-PZT): xAlN ceramics that combine improved heat transfer and pyroelectric properties for thermal harvesting applications. Detailed microstructural and compositional analysis of the materials and electrical characterization of ferroelectric and pyroelectric properties of these materials is discussed. The enhanced saturation polarization, pyroelectric coefficient, thermal conductivity, combined with the reduced relative permittivity of the composite with 0.2 wt.% AlN has demonstrated the benefits of using addition AlN to improve the heat transfer and pyroelectric properties of materials for thermal energy harvesting. The PMN-PMS-PZT: 0.2AlN ceramics exhibited a larger pyroelectric coefficient of 4146 $\mu C/m^2K$ and higher than other pure and composite counterparts. The thermal conductivity of the same sample reached 0.714 W/m°C and has improved by 9.3% compared with pristine PMN-PMS-PZT. By further comparing with

PMN-PMS-PZT: xAlN, the mechanism of enhanced heat transfer in PMN-PMS-PZT:xAlN ceramics are examined. To demonstrate the improved performance of the sample with 0.2 wt. % AlN, a pyroelectric energy harvesting system composed of a harvesting circuit was successfully demonstrated. The results clearly show that the fastest heat transfer and maximum voltage were obtained when utilizing the sample with 0.2 wt. % AlN. The measured voltage was 24.6% higher than that of the pristine PMN-PMS-PZT. The present results suggest that pyroelectric materials with the addition of AlN are highly attractive for pyroelectric sensing and energy harvesting applications.

Acknowledgements

The authors acknowledge the generous support by the National Natural Science Foundation of China under grant no. 51672092 and U1732117 and supported by Natural Science Foundation of Hubei Province of China (Grant No.2016CFB533) and Wuhan Morning Light Plan of Youth Science and Technology (No.2017050304010299).

References

1. Yan Zhang, Mengying Xie, James Roscow, Yinxiang Bao, Kechao Zhou, Dou Zhang and Chris R. Bowen, J. Mater. Chem. A, 2017, 5, 6569-6580.
2. C. R. Bowen, J.Taylor, E. LeBoulbar, D. Zabek, A. Chauhan and R. Vaish, Energy Environ. Sci., 2014, 7, 3836-3856.
3. Qiang Leng, Lin Chen, Hengyu Guo, Jianlin Liu, Guanlin Liu, Chenguo Hu and Yi Xi, J. Mater. Chem. A, 2014, 2, 11940-11947.
4. Huige Wei, Dapeng Cui, Junhui Ma, Liqiang Chu, Xiaoyu Zhao, Haixiang Song, Hu Liu, Tao Liu, Ning Wang and Zhanhu Guo, J. Mater. Chem. A, 2017, 5, 1873-1892.
5. QingpingWang, Xue Zhang, Chris R. Bowen, Ming-Yu Li, Jiahui Ma, Shiyong Qiu, Huan Liu and Shenglin Jiang, J. Alloy. Compd., 2017, 710, 869-874.

6. K.S. Srikanth, V.P. Singh and Rahul Vaish, J. Eur. Ceram. Soc., 2017, 37, 3943-3950.
7. Long Li , Xiangyong Zhao , Xiaobing Li , Bo Ren , Qing Xu , Zhu Liang , Wenning Di , Linrong Yang , Haosu Luo , Xiumei Shao , Jiaxiong Fang , Norbert Neumann , and Jie Jiao, Adv. Mater., 2014, 26, 2580-2585.
8. Fatima Zahra El Fatnani, Daniel Guyomar, M'hammed Mazroui, Fouad Belhora and Yahia Boughale, Opt. Mater., 2016, 56, 22-26.
9. Ya Yang, Wenxi Guo, Ken C. Pradel, Guang Zhu, Yusheng Zhou, Yan Zhang, Youfan Hu, Long Lin, and Zhong Lin Wang, Nano. Lett., 2012, 12, 2833-2838.
10. Xingfu Wang, Yejing Dai, Ruiyuan Liu, Xu He, Shuti Li, and Zhong Lin Wang, ACS. Nano. 2017, 11, 8339-8345.
11. An-Shen Siao, Ching-Kong Chao and Chun-Ching Hsiao, Sensors, 2015, 15, 19633-19648.
12. Ian M. McKinley, Felix Y. Lee, Laurent Pilon, Appl. Energ., 2014, 126, 78-89.
13. Daniel Guyomar, Gaël Sebald, Sébastien Pruvost, Mickaël Lallart, Akram Khodayari and Claude Richard, J. Intel. Mat. Syst. Str., 2009, 20, 609-624.
14. Daniel Guyomar and Mickaël Lallart, J. Appl. Microbiol., 2009, 86, 1-10.
15. Ugur Erturun, Christopher Green, Matthew L Richeson and Karla Mossi, J. Intel. Mat. Syst. Str., 2014, 25, 1838-1849.
16. Chun-Ching Hsiao, Jing-Chih Ciou, An-Shen Siao and Chi-Yuan Lee, Sensors, 2011, 11, 10458-10473.
17. Chun-Ching Hsiao, An-Shen Siao and Jing-Chih Ciou, Sensors, 2012, 12, 534-548.
18. Chun-Ching Hsiao and An-Shen Siao, Sensors, 2013, 13, 12113-12131.
19. Mengying Xie, Daniel Zabek, Chris Bowen, Mostafa Abdelmageed and Mustafa Arafa. Smart Mater. Struct., 2016, 25, 125023-125030.
20. Zhidong Hana and Alberto Fina. Prog. Polym. Sci., 2011, 36, 914-944.
21. Yuan-Xiang Fu, Zhuo-Xian He, Dong-Chuan Mo and Shu-Shen Lu, Appl.

Therm. Eng., 2014, 66, 493-498.

22. Shyan-Lung Chung and Jeng-Shung Lin, Molecules. 2016, 21, 670-680.
23. Zhaofu Wang, Rong Qi, Jin Wang and Shuhua Qin, Ceram. Int., 2015, 41, 13541-13546.
24. Jianwen Xia, Guoping Zhang, Libo Deng, Haipeng Yang, Rong Sun and Ching-Ping Wong, RSC Adv., 2015, 5, 19315-19320.
25. Jian Jiao, Yonghong Cui and Yu Xia, High Perform. Polym., 2017, 29, 484-492.
26. Wenhui Yuan, Qiangqiang Xiao, Li Li and Tao Xu, Appl. Therm. Eng., 2016, 106, 1067-1074.
27. Chi Zhang, Xiumin Yao, Yinsheng Lia, Hanqin Liang, Jian Chen, Jingxian Zhang, Jian Yang, Xiaoyun Li, Tai Qiu, Zhongming Chen, Xuejian Liu and Zhengren Huang, Ceram. Int., 2015, 41, 9107-9114.
28. Shenglin Jiang, Pin Liu, Xiaoshan Zhang, Ling Zhang, Qi Li, Junlong Yao, Yike Zeng, Qing Wang and Guangzu Zhang, J. Alloy. Compd., 2015, 636, 93-96.
29. E. Crisman, A. Drehman, R. Miller, A. Osinsky, D. Volovik, and V. Vasilyev, Phys. Status Solidi C, 2014, 11, 517-520.
30. Yuan-Yuan Tang, Peng-Fei Li, Wan-Ying Zhang, Heng-Yun Ye, Yu-Meng You and Ren-Gen Xiong, J. Am. Chem. Soc., 2017, 139, 13903-13908.
31. B Hanrahan, L Sanchez, C M Waits and R G Polcawich, Smart Mater. Struct., 2016, 25, 015025-015034.

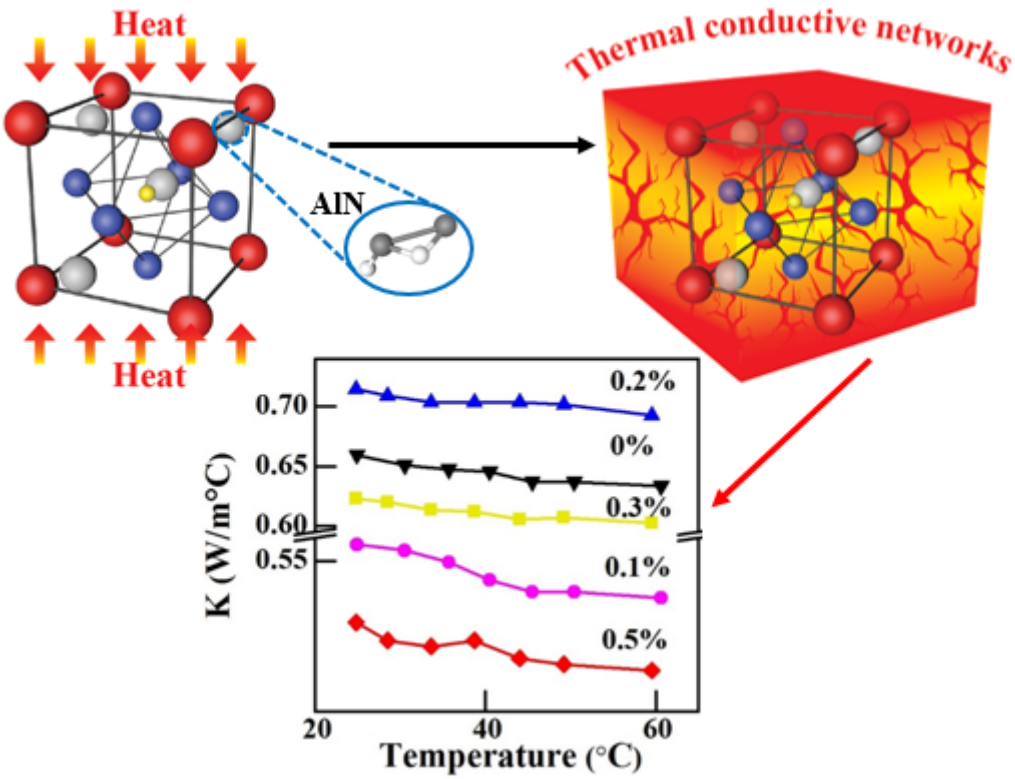

Table of contents

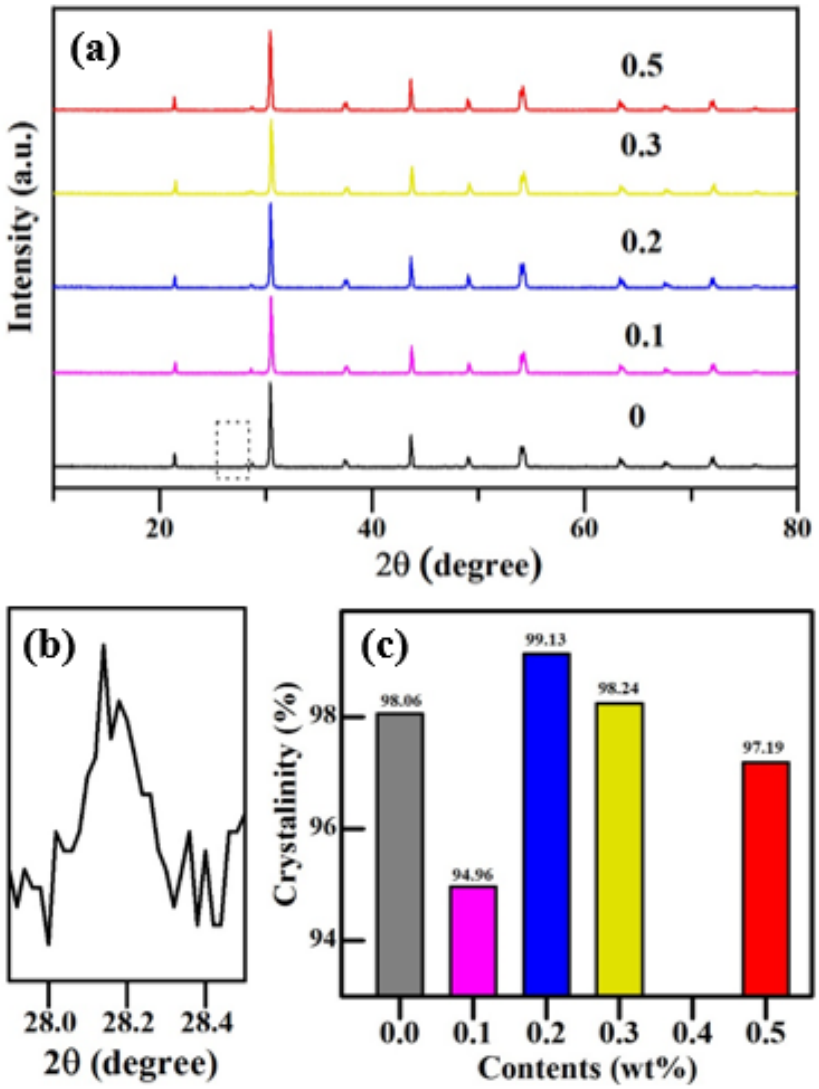

Fig. 1. (a) X-ray diffraction (XRD) spectra of the samples with a variation of AlN contents: 0, 0.1, 0.2, 0.3, 0.5 wt.%. (b) Expanded patterns for the 2θ range between 27.9 and 28.5° for a material with x = 0 wt.%. (c) Crystallinity of the samples with a variation of AlN contents: 0, 0.1, 0.2, 0.3, 0.5 wt.%.

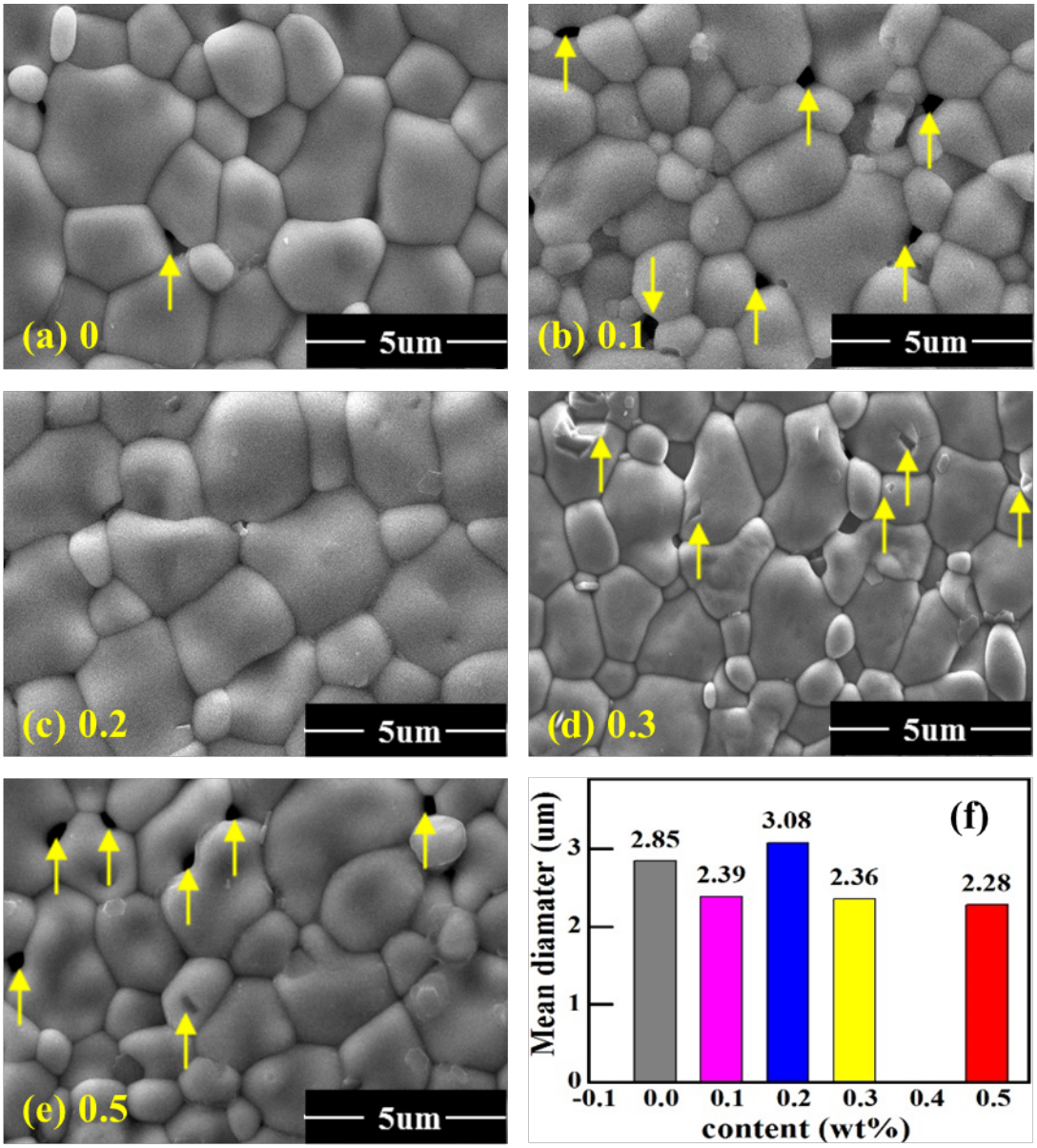

Fig. 2. Scanning Electron Microscopy (SEM) *images of the samples PMN-PMS-PZT*: xAlN: (a) x = 0, (b) x = 0.1, (c) x = 0.2, (d) x = 0.3, (e) x = 0.5 wt.%, (f) Mean grain diameter size distribution histogram of the materials with various AlN contents.

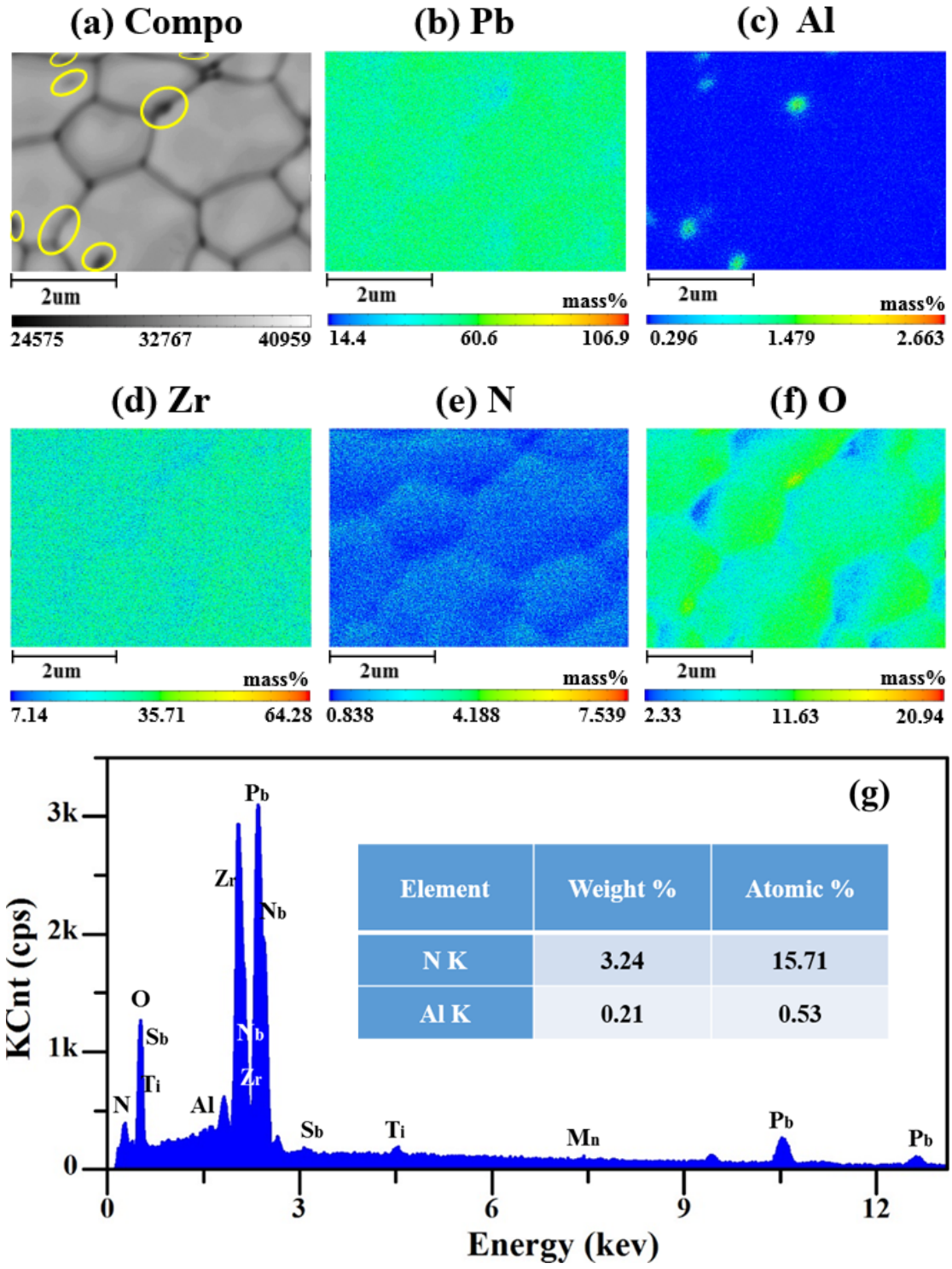

Fig. 3. Elemental analysis of *the* PMN-PMS-PZT: 0.2AlN *sample*. (a) SEM image of microstructure. Elemental distribution of (b) Pb, (c) Al, (d) Zr, (e) N, and (f) O. (g) The energy-dispersive spectrum of the PMN-PMS-PZT: 0.2AlN s*ample*.

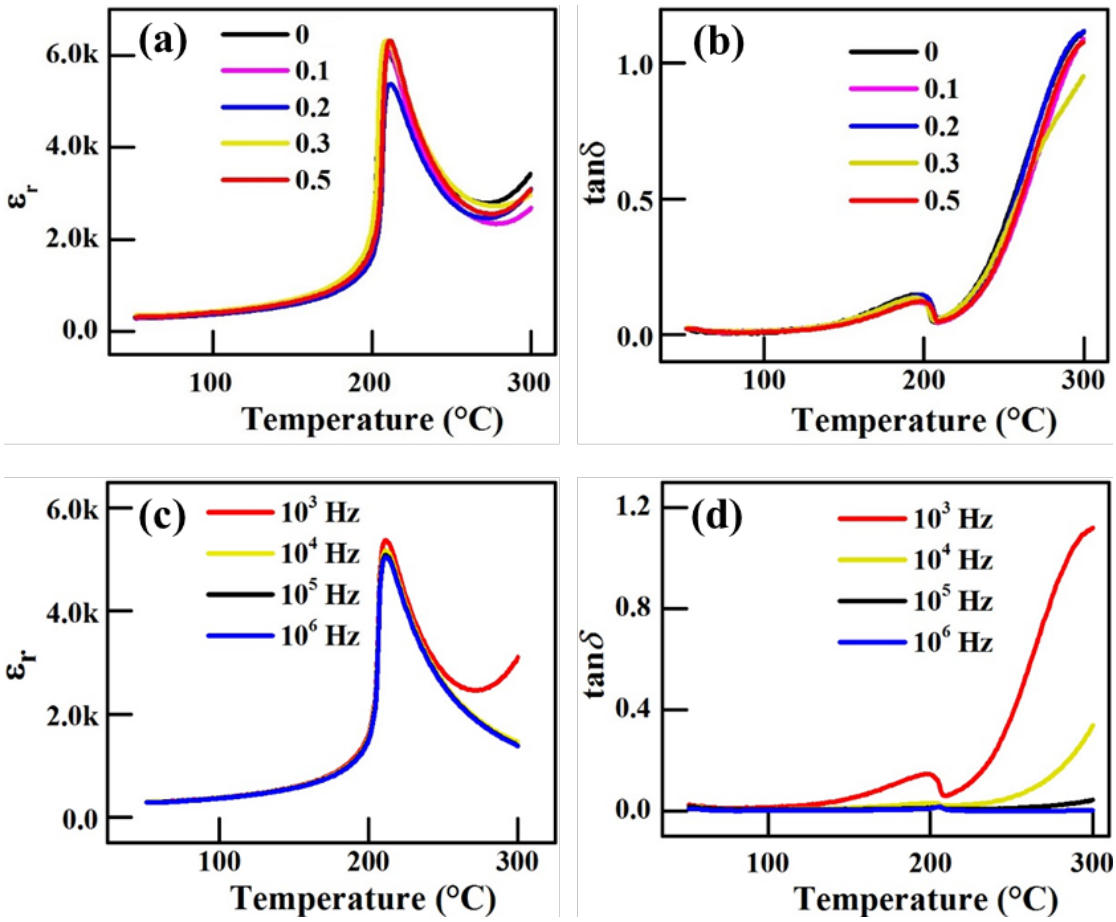

Fig. 4. Temperature-dependent dielectric properties of the PMN-PMS-PZT: AlN *materials with various AlN contents:* 0, 0.1, 0.2, 0.3, 0.5 wt.%. (a) Temperature-dependent relative permittivity (dielectric constant) and (b) dielectric loss of the corresponding materials at 1 kHz. (c) The temperature-dependent relative permitivity (dielectric constant) and (d) dielectric loss of the samples with x = 0.2 wt% at different frequencies.

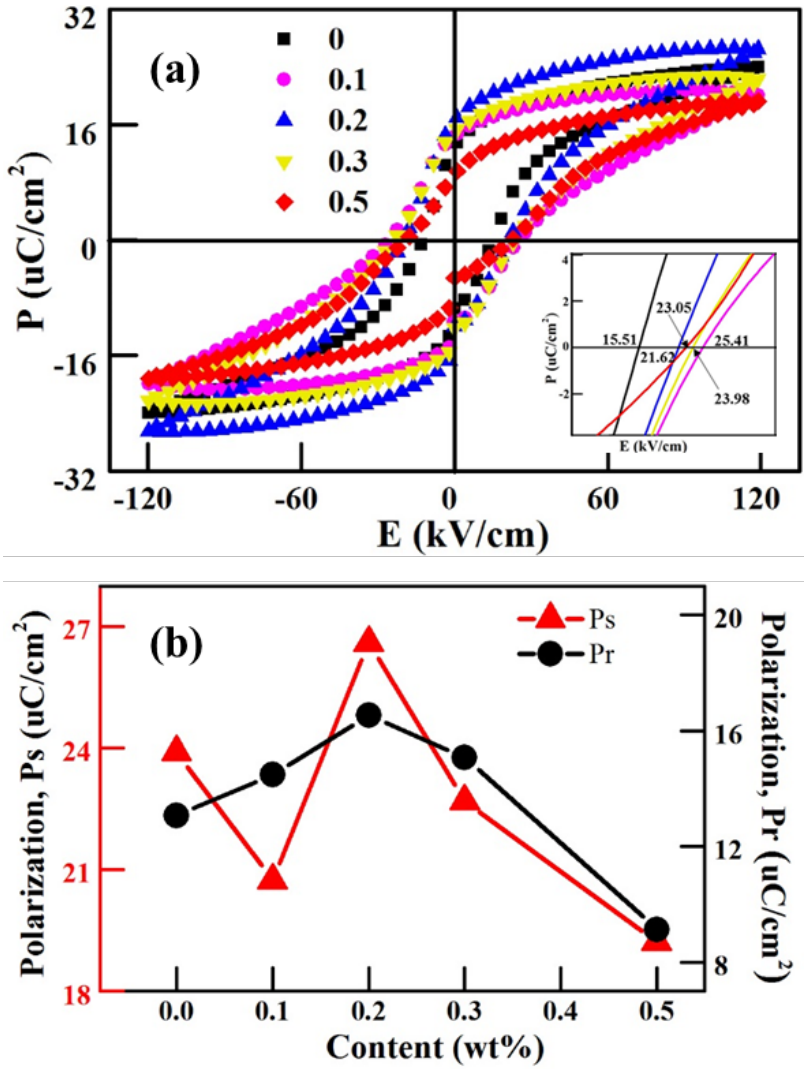

Fig. 5. Room-temperature ferroelectric properties *of the PMN-PMS-PZT*: xAlN samples: x = 0, x = 0.1, x = 0.2, x = 0.3, x = 0.5 wt.%. (a) P-E loops with different AlN additions and (b) Saturation polarization (P_s) and remnant polarization (P_r) values for the samples with various AlN contents.

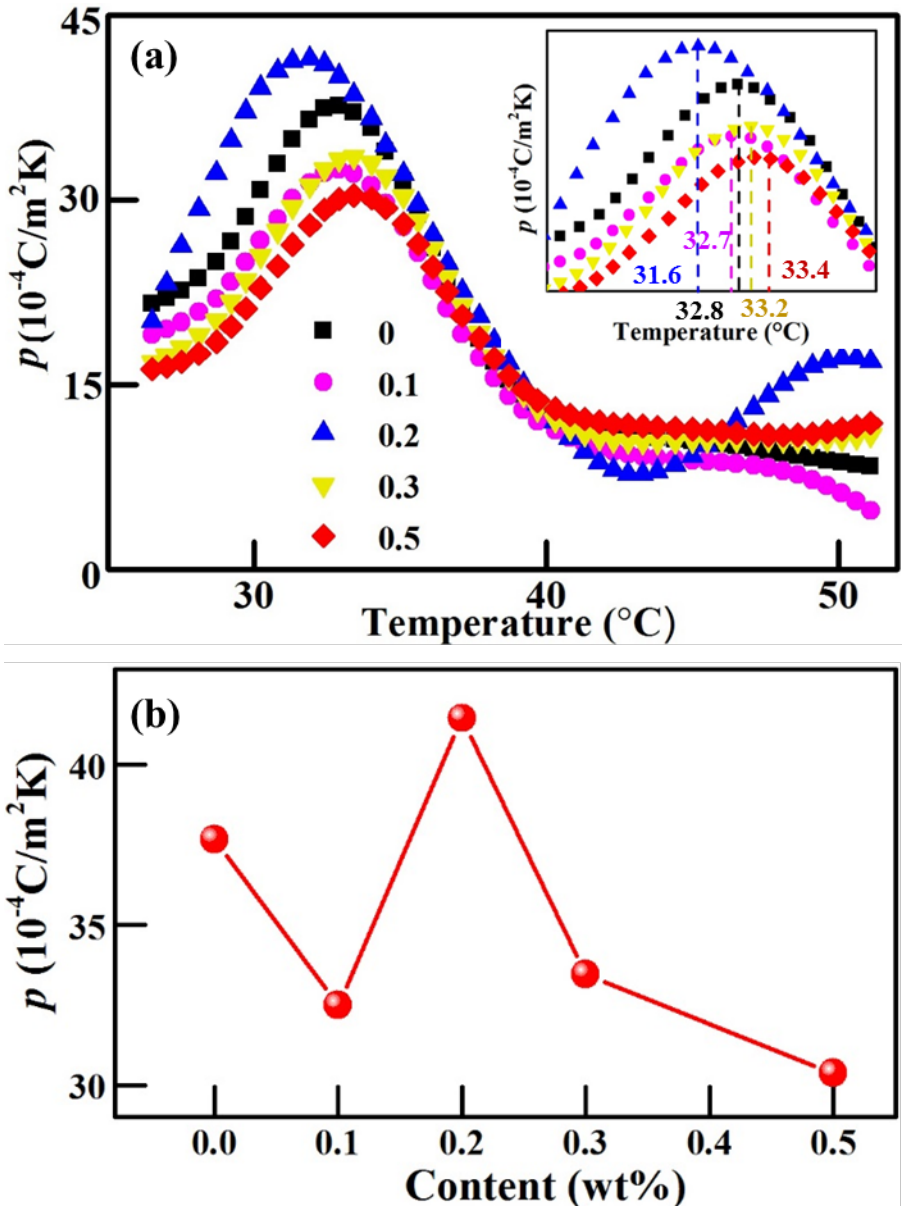

Fig. 6. (a) Tempearture-dependent pyroelectric coefficient of the PMN-PMS-PZT: AlN *samples with various AlN contents:* 0, 0.1, 0.2, 0.3, 0.5 wt.%. (b) Values of the pyroelectric coefficient (*p*) for the corresponding samples.

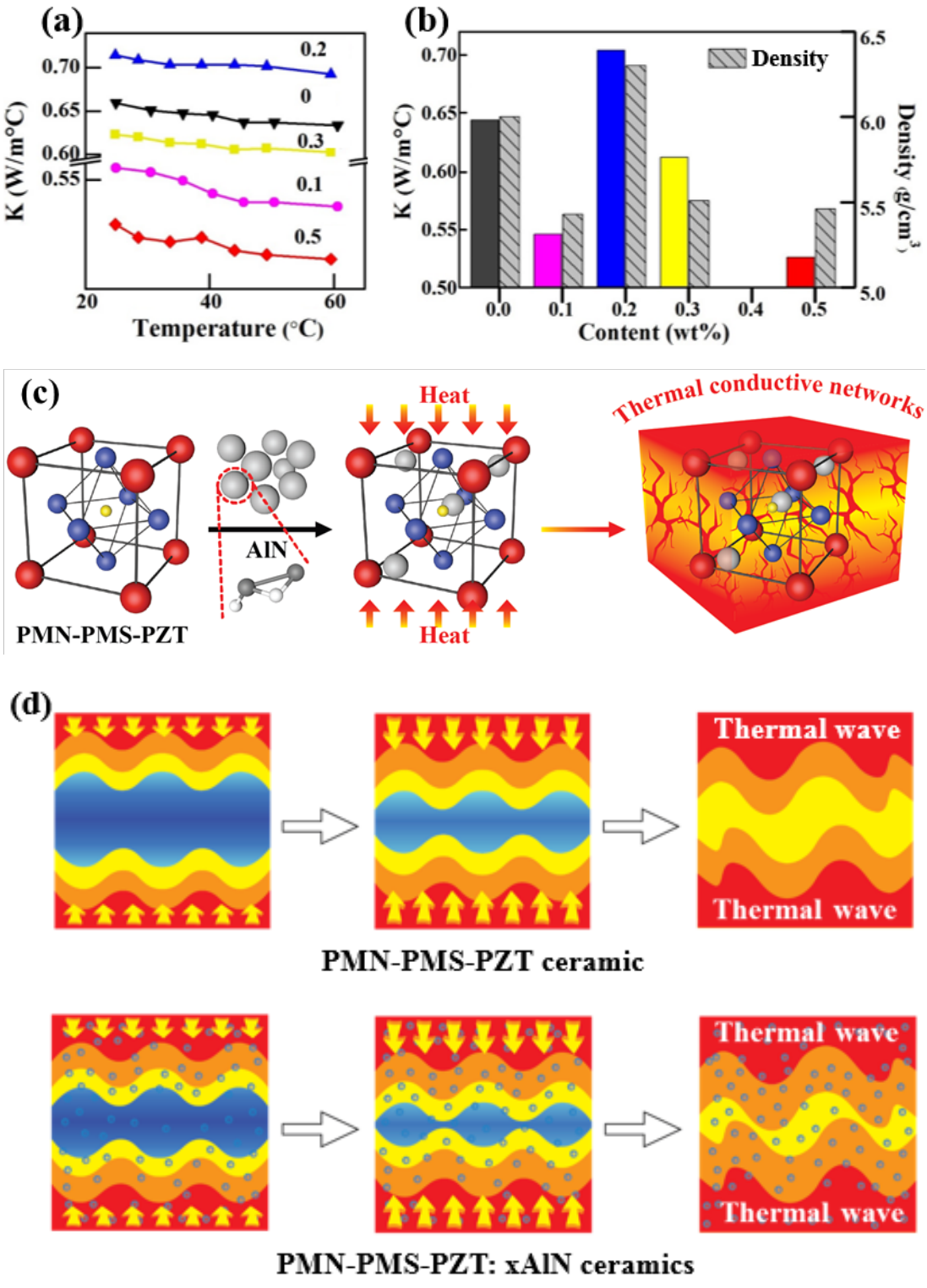

Fig. 7. (a) Thermal conductivity as a function of temperature. (b) Thermal conductivity and density of the samples with various AlN contents: 0, 0.1, 0.2, 0.3, 0.5 wt. %. (c) Heat transfer model in the PMN-PMS-PZT: xAlN ceramics. (d) Mechanism of the heat transfer.

Think there need to be clarity on the mechanism.

(c) seems to indicate that the AlN is mixing on the atomic scale (solid-solution) to form compounds?

(d) seems to indicate the AlN are discrete particles (ie. not mixing at the atomic scale) and this higher thermal conductivity create a thermal network.

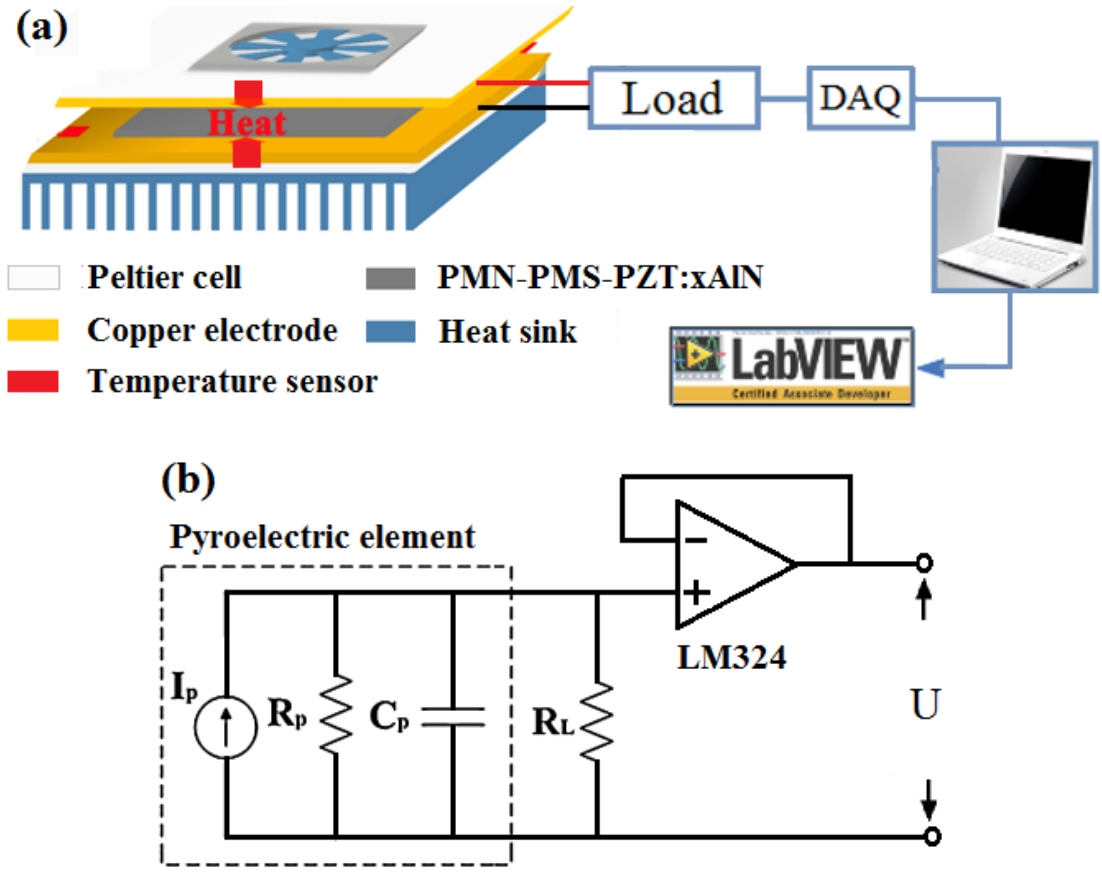

Fig. 8. (a) Schematic of measurement setup and (b) circuit for pyroelectric energy harvesting.

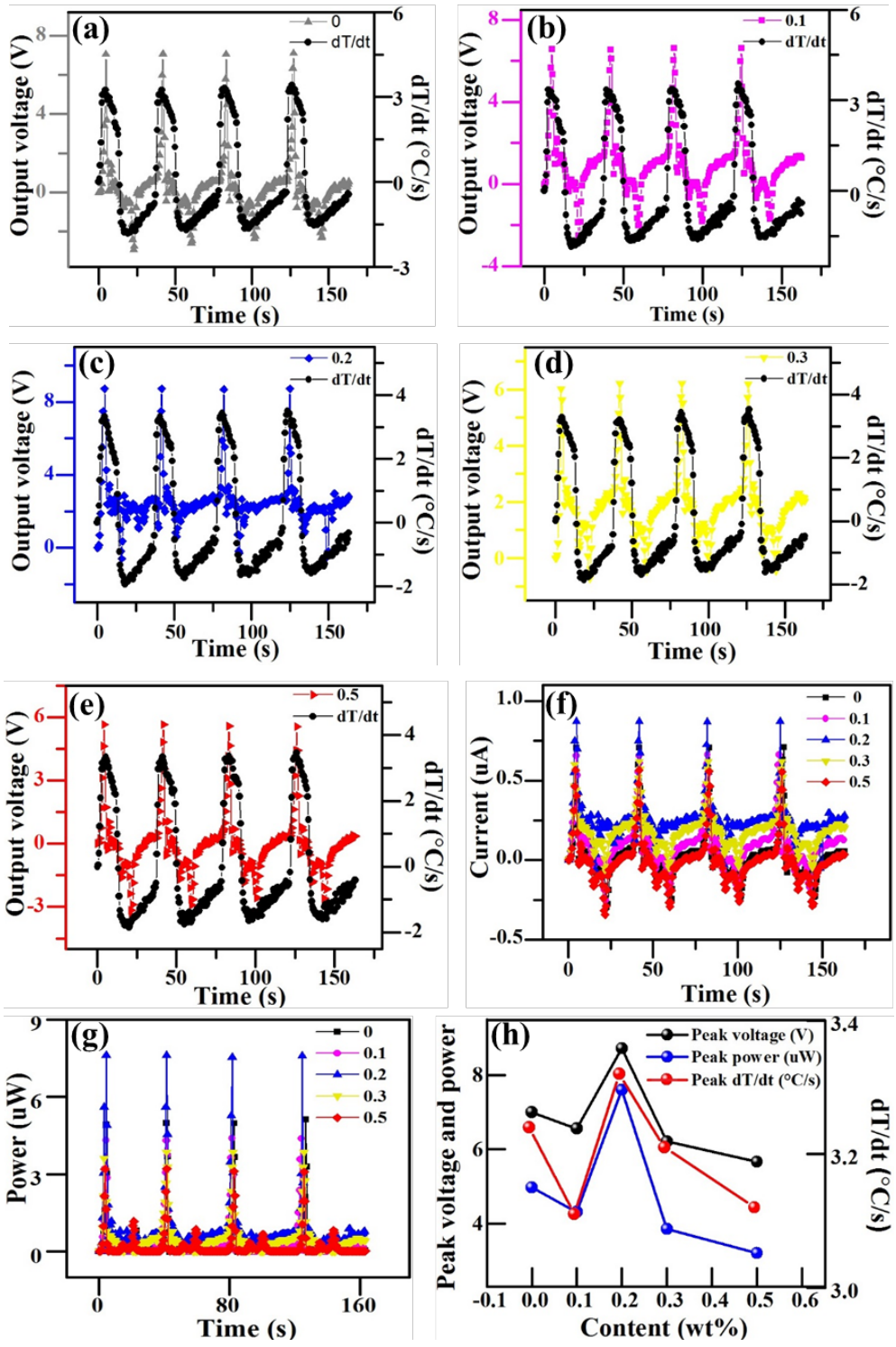

Fig. 9. (a) Output voltage and rate of temperature change for the samples with 0 wt.% (a), 0.1 wt.% (b), 0.2 wt.% (c), 0.3 wt.% (d), and 0.5 wt.% (e) AlN contents, respectively, (f) Output current and (g) Output power as a function of the AlN contents. (h) Plots of the corresponding peak voltage, power and dT/dt.